

## Research Article

# Three-Dimensional Reconstruction of Rolling Contact Fatigue Characteristics

Chengkai Zeng , Gaopeng Xu , Hai Li , Gang Zhu , and Yan Yang 

College of Mechanical Engineering, Chongqing University of Technology, 69 Hongguang Ave, Chongqing 40005, China

Correspondence should be addressed to Yan Yang; yangyan@cqut.edu.cn

Received 25 October 2021; Revised 30 December 2021; Accepted 31 December 2021; Published 24 January 2022

Academic Editor: Xiaowei Li

Copyright © 2022 Chengkai Zeng et al. This is an open access article distributed under the Creative Commons Attribution License, which permits unrestricted use, distribution, and reproduction in any medium, provided the original work is properly cited.

Focusing on the 3D topographic characteristics of rolling contact fatigue, a reconstruction method of the fatigue surface of roller based on point cloud data was proposed in this research. A 3D laser scanner was used to capture the data of point cloud on the surface of the fatigue roller. The gradient segmentation method was used to achieve segmentation of the fatigue contact surface, and the Kd-Tree algorithm in Statistical Outlier Removal filter was adopted to remove different types of noise. The greedy triangulation and hole repair and reconstruction of the curled point cloud were conducted. The experimental results showed that the segmentation accuracy of the fatigue contact surface was above 97.7%, the curling error rate of point cloud was 0.09%, and the maximum deviation of the reconstructed fatigue roller surface was 0.0199 mm. These methods can be applied to analyze the working conditions of roller specimen and contact fatigue.

## 1. Introduction

Contact fatigue is a kind of surface fatigue damage phenomenon in which the contact surface of contact material forms pits with the influence of long-term cyclic contact stress [1, 2]. In engineering fields, such as machinery, vehicles, ships, and aviation, some parts under rolling contact conditions, such as rolling bearings, shafts, cams, and gears, which often fail due to contact fatigue, are frequently used [3, 4]. According to statistics, 80% to 95% of mechanical failures were the results of metal fatigue. The annual GDP loss is as high as 4% worldwide [5–7]. Hence, accurate acquisition of the contact fatigue performance parameters of metal materials is of great significance to prevent contact fatigue accidents [8, 9]. In addition, methods to determine fatigue failure in the fatigue contact test are mainly realized through human eye observation, vibration signal, temperature signal, friction torque signal analysis, and acoustic emission detection [10–12]. The direct detection method is manual visual detection. The rest are the indirect detection method. Although they are widely used at present, they all are unable to quantify the problem of fatigue pitting defect information and visualize issues, such as fatigue status.

In order to obtain the capability to detect and identify the fatigue defects of parts in real time and in an accurate manner, the machine vision-based detection technology has been introduced for the rolling contact fatigue test. Sun et al. [13] made use of neighborhood weighted segmentation to extract surface defects and detected cam-shaft surface defects, which has been a success. Xie et al. [14] came up with an algorithm to extract key parameters of carrot surface defects based on machine vision. In this case, carrot surface defect detection and online classification have been realized. Nirbhar et al. [15] came up with a global adaptive threshold method based on gradient images to detect steel surface defects. Given that this method failed to pay sufficient attention to the local features of the image during the threshold selection process, the edges of some defects were not correctly identified. In addition, an improved Otsu algorithm based on automatic weighted threshold proposed by Xu et al. [16] can achieve a good segmentation of rolling contact fatigue defect detection. The above detection methods only detect the surface defects of the workpiece in two dimensions, without detecting important information such as the three-dimensional shape of the defect, or

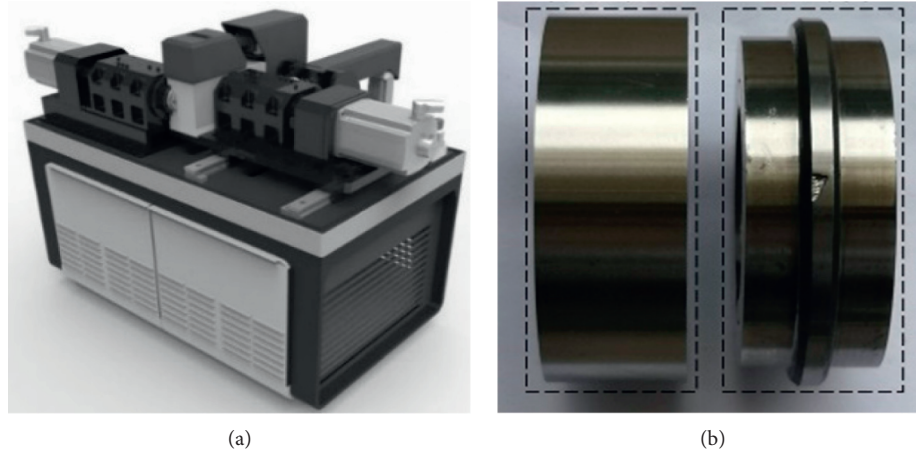


FIGURE 1: Test equipment and samples. (a) Contact fatigue testing machine and (b) main specimen and companion specimen.

visualize the defects. Certainly, these methods have limitations.

The 3D reconstruction technology based on machine vision features high accuracy, good real time performance, and fast speed [17, 18]. Scholars at home and abroad have performed extensive research on it. Although the 3D reconstruction technology based on machine vision has been widely used in various fields, there is no research on its application in rolling contact fatigue test. The 3D reconstruction technology in other fields can be used as references. Snavely et al. [19] developed an interactive 3D reconstruction system. The system is able to automatically calculate the viewpoint of each photo and the sparse model between the scene and the image. Nonetheless, the reconstruction effect is not clear enough and the degree of visualization is low, which are the disadvantages. Furukawa et al. [20] proposed a method to obtain a complex 3D model from multiple calibrated pictures. Microsoft Research launched the Kinect Fusion project [21], in which the Kinect sensor was used for the sake of acquiring the depth image data of the scene in multiple directions, and reconstructing the 3D model of the scene in real time. Microsoft Research announced the Mobile Fusion project [22] to collect data through the mobile phone RGB camera. Also, reconstruction technology can be used to complete the reconstruction of the target object. In the current rolling contact fatigue test, the acquired fatigue pitting defect information is not perfect. Problems such as the inability to visualize the fatigue pitting corrosion state and display the three-dimensional morphological characteristics of the sample after failure are both important issues.

A method of 3D topography reconstruction of the fatigue roller surface based on point cloud data was conducted for the sake of resolving the problems above. The method in the present study is based on point cloud data and researches the processing algorithm of 3D point cloud data. A denoising algorithm for the fatigue roller surface point cloud based on conditions and statistics was designed aiming at the different types of noise in the roller surface point cloud data. The algorithm can improve the quality of the point cloud. In order to realize the reconstruction of the three-dimensional

topography of the fatigue roller surface, this paper studies the 3D reconstruction algorithm, which can visualize the three-dimensional topography of the failure surface of the roller sample. Then the experimental results of the three-dimensional shape reconstruction of the roller sample are illustrated and analyzed. Some discussions and conclusions are given finally.

## 2. Fatigue Test System

Figure 1(a) shows the contact fatigue testing machine developed by our research group. It collected sample surface information in real time through the image acquisition system. Figure 1(b) shows the original image of the sample. Then the collected images have been analyzed after computer processing. After that, users may determine whether the sample has fatigue failure according to the result. The machine will be shut down immediately when the fatigue goes beyond the standard. This machine made use of 2D image area to judge failure. In addition, the 3D topographic characteristics of rolling contact fatigue are an urgent need as per the deep research on the failure.

## 3. Methods

### 3.1. Data Collection and Preprocessing

**3.1.1. Point Cloud Data Acquisition.** In recent years, 3D laser scanning technology has developed rapidly. 3D reconstruction based on point cloud data has long become a hot and thought-provoking research topic [23–25]. The 3D laser scanning technology made use of noncontact active measurement method to collect point cloud data, which has the characteristics of strong real time, fast scanning speed, and high precision. For the rolling contact fatigue test, in the present study, the fatigue failure of the roller specimen was taken as the research object. The Gocator2420 laser scanners produced by the LMI Technologies company (LMI) was used to obtain the three-dimensional information of the fatigue roller surface. The intact and defect-free standard roller surface were firstly used as the reference surface before

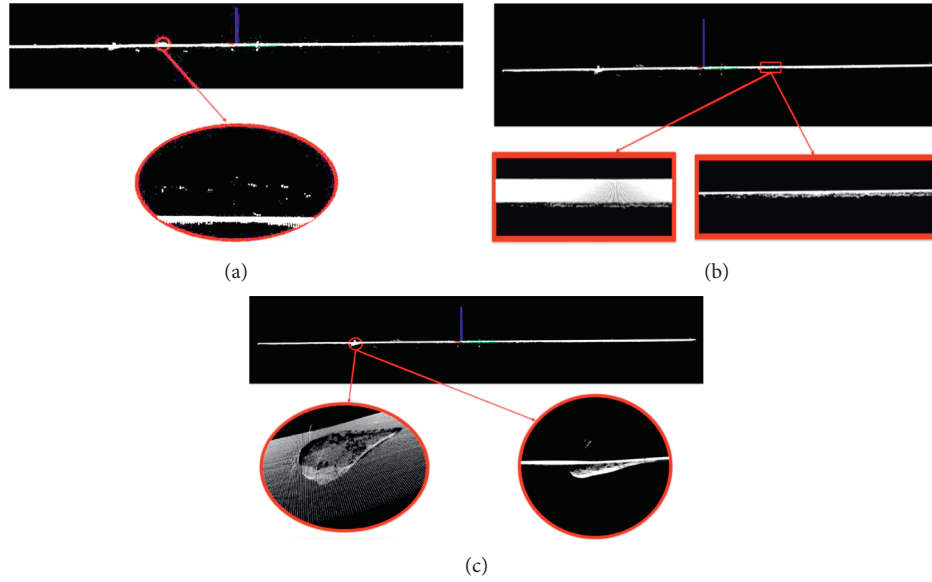


FIGURE 2: Types of noise points on the surface of fatigue rollers. (a) YZ plane view of isolated point, (b) different angle views of noise on the chamfered edge, and (c) different angle views of outlier noise.

acquiring the point cloud data. After that, the Z-direction zero value was calibrated via the software equipped with the laser sensor. Then the external encoder pulse signal was used at appropriate speed to trigger the laser scanner and scan the surface of the test piece. Finally, the original point cloud image of the test piece was obtained.

### 3.1.2. Data Preprocessing

*Fatigue Contact Surface Segmentation.* High accuracy of the Gocator laser scanner contributes to large amount of point cloud data acquired. Too much point cloud data tends to reduce the operating speed of the computer. Therefore, it is necessary to segment the point cloud of the fatigue contact surface from the acquired point cloud data. It can be found that the roller boss part is the fatigue contact surface upon the analysis of the roller structure and the original data. Also, the fatigue contact surface point cloud and the nonfatigue contact surface point cloud in the point cloud data obtained are not in the same plane, but in the Z-axis direction. Besides, a certain gradient is present, which is shown in Figure 1. Hence, this present study made use of gradient segmentation [26] to extract the point cloud data of fatigue contact surface. Given that the origin of the point cloud is at the center of the original point cloud, the X coordinates of the points where the Z-direction coordinate changes on the original point cloud graph were counted respectively. Also, the average values of the X coordinates of these sudden changes were calculated respectively as the upper and lower thresholds of the gradient segmentation. The expression of the gradient segmentation function to extract the point cloud data of the fatigue contact surface is

$$ds t(x, y, z) = \begin{cases} \text{src}(x, y, z), & t \leq x \leq T, \\ 0, & \text{otherwise,} \end{cases} \quad (1)$$

where  $\text{src}(x, y, z)$  is the original coordinate of the point cloud and  $t$  and  $T$  are the upper and lower thresholds of gradient segmentation, respectively.

*Point Cloud Denoising.* The above method was used to segment and extract the obtained fatigue roller surface point cloud data. However, some noises can still be heard in the extracted roller fatigue contact surface point cloud owing to the influence of equipment and external environmental factors, such as light, vibration, and occlusion. These factors have been proven to be able to affect the segmentation and extraction of point cloud data and reduce the quality of point cloud. According to the analysis of the obtained point cloud image of the fatigue roller surface, it has been found that these noises mainly exist in three types: solitary points, chamfer edge noise, and outlier noise, as shown in Figures 2(a)–2(c).

In the present research, after analyzing the types of noise points on the point cloud on the surface of the fatigue roller, a set of denoising algorithms was designed specifically for the point cloud on fatigue roller surface. After that, a standard roller sample was further used as a calibration part to calibrate the measurement system before obtaining the point cloud data. The removal of different types of noise on the surface of the fatigue roller has been achieved through a combination of conditions and statistics. Among them, for isolated points and chamfer edge noise, the value of the point cloud coordinate axis direction is used as the judgment condition by setting corresponding conditions, thus realizing the removal of these two types of noise.

For outlier noise points, the average distance from each point to its neighbors is counted. In addition, the result approximately conformed to the Gaussian distribution. The distribution of adjacent point clouds shows a feature of symmetry and uniformity. The probability density function is

$$f(x_i) = \frac{1}{\sqrt{2\pi}\sigma} \exp\left(-\frac{(x_i - \mu)^2}{2\sigma^2}\right), \quad (i = 1, 2, 3, \dots), \quad (2)$$

where  $x_i$  is the average distance of the neighborhood of any point,  $\mu$  is the mean value of the average distance of the neighborhood, and  $\sigma$  is the standard deviation.

Given that outlier noise features uneven density and relatively sparse property, the calculation of the distance distribution from one point to its adjacent point in the input data can be used to eliminate the noise. Hence, the Kd-Tree algorithm in the Statistical Outlier Removal filter [27] was used to remove outlier noise. First traverse the point cloud and find the  $K$  adjacent points corresponding to each point  $P_i(x_i, y_i, z_i)$  ( $i = 1, 2, \dots, n$ ). For each point, calculate the average distance from it to all its adjacent points; remove the points with the average distance from  $K$  adjacent points exceeding the standard range  $D$ ,  $D = \mu \pm \alpha\sigma$ , and  $\alpha$  is a constant, which is a multiple of the standard deviation. The average distance  $d_i$ , mean  $\mu$ , and the calculation expression of standard deviation  $\sigma$  is

$$d_i = \frac{1}{k} \sum_{j=1}^k \sqrt{(x_i - x_j)^2 + (y_i - y_j)^2 + (z_i - z_j)^2}, \quad (3)$$

$$\mu = \sum_{i=1}^n \frac{1}{n} d_i, \quad \sigma = \sqrt{\frac{1}{n} \sum_{i=1}^n (d_i - \mu)^2}.$$

### 3.2. 3D Reconstruction of the Fatigue Roller Surface

**3.2.1. Point Cloud Curling.** Given that the test piece is a rotating body roller specimen, point cloud crimping was come up with to make the reconstruction result consistent with the original specimen shape:

- (1) Find the curl radius  $R$ : first, obtain the point with the largest absolute value of the coordinate in the  $Y$ -axis direction of the point cloud according to the input point cloud image. This point is the end point of the input point cloud image. Since the coordinate origin of the input point cloud image is at the center of the point cloud image, the  $Y$  coordinate value of the end point is half the circumference of the point cloud, so the radius  $R$  after rolling up is obtained.
- (2) Find the radian: take the point cloud coordinate origin  $O$  as the starting point of the first curl, find the radian value  $\alpha_i$  corresponding to the arc length from any point  $P_i(x_i, y_i, z_i)$  ( $i = 1, 2, \dots, n$ ) to this point, and find the sine  $\sin \alpha_i$  and cosines  $\cos \alpha_i$  corresponding to the angle, where  $\alpha_i = (L_i/R)$ , ( $i = 1, 2, \dots, n$ ).
- (3) Find the center of the curling circle: take the point  $O$  and let it be perpendicular to the  $XY$  plane, with the point with a length of  $R$  as the center of the first curling circle. The obtained center coordinates are the  $X$  and  $Y$  coordinates of the origin point cloud. Add  $R$  to the coordinate value.

- (4) Point cloud curling: the curling process is actually the process of point cloud coordinates changing. Take the first circle of curling as an example, where the  $X$  coordinate of each point remains unchanged. The  $Y$  coordinate of each point is the curl radius plus the distance from each point in the  $Z$  direction to the starting point in the  $Z$  direction, multiplied by its sine value, and finally the center coordinate  $Y$  value is added. The  $Z$  coordinate of each point is the curl radius plus the distance from the  $Z$  direction of each point to the  $Z$  direction of the starting point, multiplied by the cosine value, and finally the center coordinate  $Z$  value, thus completing a circle of point cloud curling.
- (5) Change the coordinates of the center of the circle, traverse all the points, then repeat step (4). In this way, the point cloud would be curled.

**3.2.2. Point Cloud Gridding.** The current surface reconstruction methods based on point cloud data are divided into three categories mainly: implicit surface reconstruction [28], parametric surface reconstruction [29], and mesh surface reconstruction [30]. In the present study, the mesh surface reconstruction method based on the greedy algorithm is used to triangulate the preprocessed point cloud to reconstruct the three-dimensional mesh surface of the fatigue roller.

The greedy triangulation algorithm is a fast and efficient method for 3D surface reconstruction. It projects 3D points to the corresponding plane through the normal direction to triangulate, thereby obtaining the topological structure between the original 3D points. The algorithm steps are as follows:

- (1) Let the point cloud data set be  $Q = \{Q_i, i = 1, 2, 3, \dots, n\}$ . Use  $k$ -d tree to establish spatial neighborhood index.
- (2) Choose one of the points  $Q_i$  as the starting point, and use the point and its  $k$  adjacent points to fit the point-domain normal vector  $N$ . From the point and the normal vector  $N$ , the tangent plane of the point can be obtained.
- (3) Project the point  $Q_i$  and its  $k$  adjacent points on the plane  $V_1$ , obtain the original point  $Q_j$  corresponding to the nearest point of the point  $Q_i$  according to the neighboring relationship of the projected point, and connect with  $Q_i$  and  $Q_j$  as the starting edge of the triangulation.
- (4) Fit the tangent plane from the connection between  $Q_i$  and  $Q_j$  and the adjacent points to acquire the tangent plane  $V_2$ .
- (5) Project the adjacent points near the line  $Q_i Q_j$  segment onto the plane, then use the Delaunay triangulation method to find the corresponding third original point  $Q_k$ , and connect the three points to form the first triangle.

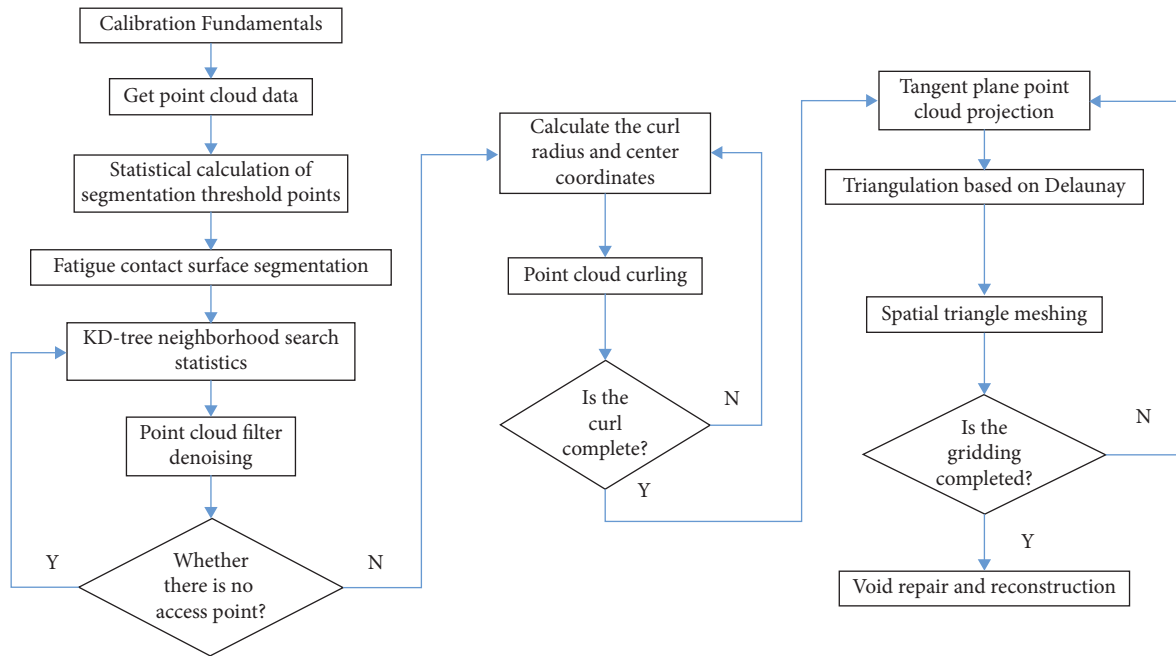


FIGURE 3: Flow chart of point cloud processing and 3D reconstruction.

- (6) The three sides of the first triangle are taken as the starting side, then repeat step (5) to traverse all the spatial points to complete the point cloud gridding.

**3.2.3. Point Cloud Hole Repair and Reconstruction.** Holes show up in the missing parts of the point cloud data after point cloud gridding. The quality of the reconstruction would be directly affected if these missing areas were not repaired [31]. There are two main types of hole repair methods in 3D reconstruction. One type of methods is the hole repair based on scattered point clouds [32]. The other type is the repair of surface holes based on triangular meshes [33]. To create a surface patch, the hole repair based on scattered point cloud is based on the scattered points at the boundary of the hole. This repair method is suitable for surfaces with small curvature changes, while the surface hole repair based on triangular meshes tends to present more uniform distribution of point clouds. The curved surface has a remarkable effect. The repair has been implemented in the present study Geomagic Studio software. The repair and reconstruction process mainly uses meshing to find the boundary of the hole and fill the hole based on the curvature. According to the reconstruction results, the shape characteristics of the roller fatigue contact surface have been soundly maintained, marking an important support for analyzing the contact fatigue performance of the roller specimen under simulated working conditions.

## 4. Results and Discussion

**4.1. Test Conditions.** In order to verify the point cloud processing method and reconstruction effect for rolling contact fatigue rollers proposed in the present study, 4 types of fatigue rollers with different widths and different fatigue

effects were selected for experimental tests. The test process is to install VS2015 on a PC with 3.2 GHz processor and 8 GB memory and, on this basis, configure the PCL1.8.0 environment. The overall flow chart of point cloud processing and 3D reconstruction are shown in Figure 3.

**4.2. Denoising Results of Point Cloud on the Fatigue Roller Surface.** The choice of the value of  $k$  and  $\alpha$  will directly affect the denoising effect. If the selected value of  $k$  is too large or the value of  $\alpha$  is too small, the denoising would be prone to becoming excessive denoising. If the selected value of  $k$  is too small and the value of  $\alpha$  is too large, the denoising effect will not be good. This paper uses many different experiments to determine the appropriate value of  $k$  and  $\alpha$ . The denoising effect tends to be better as the  $k$  value is selected in the range of 20–40. Similarly, when the  $\alpha$  value is selected in the range of 1–3, the denoising effect is better. The experimental pictures are shown in Figure 4 in the range of  $k$  and  $\alpha$ . Table 1 shows the experimental data. In addition, according to the effect of these pictures, when  $k=40$ ,  $\alpha=1$ , part of the point cloud at the pitting defect is regarded as the excessive point. When  $k=20$ ,  $\alpha=3$ , the noise at the pitting defect is not completely removed, and there are still noises at the position of the yellow circle in the picture. The denoising results of point cloud on fatigue roller surface show up as  $k=30$  and  $\alpha=2$ .

The point cloud of the four types of fatigue roller contact surface after segmentation is shown in Figures 5(a), 6(a), 7(a), and 8(a). By means of the condition and statistics-based method of denoising the point cloud of the fatigue roller surface in the present study, the noise points in the point cloud have undergone denoising experiments. The experimental results are shown in Figures 5(b), 6(b), 7(b), and 8(b).

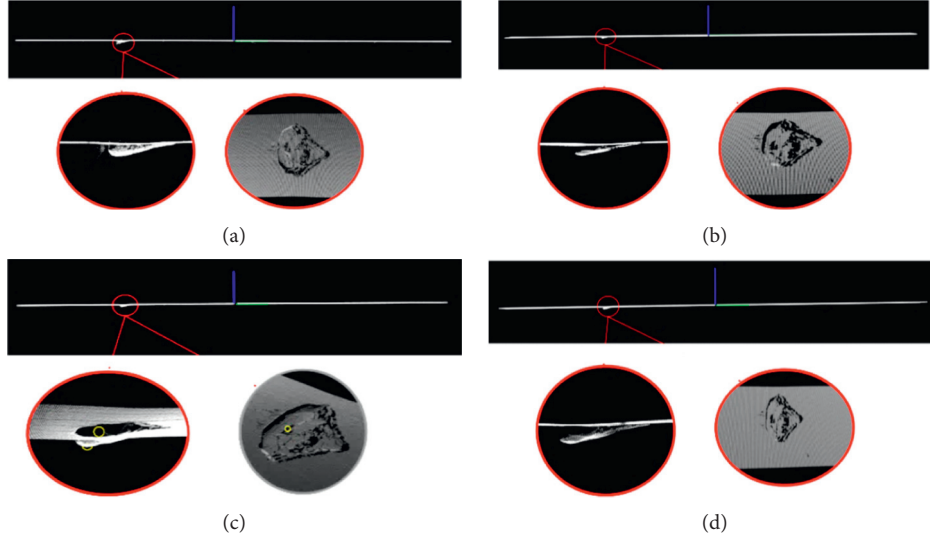


FIGURE 4: Denoising effect of discrete noise on the contact surface of fatigue roller with different parameters. (a) Discrete noise map of fatigue roller contact surface; (b) denoising effect picture when  $k=40$  and  $\alpha=1$ ; (c) denoising effect picture when  $k=20$  and  $\alpha=3$ ; and (d) denoising effect picture when  $k=30$  and  $\alpha=2$ .

TABLE 1: Comparison of noise reduction with different  $K$  values and  $\alpha$  values.

| $K$ | $\alpha$ | Number of point clouds after denoising/piece | Denoising ratio/% |
|-----|----------|--|-------------------|
| 40  | 1        | 871872                                       | 3.231             |
| 40  | 2        | 883319                                       | 1.961             |
| 40  | 3        | 892701                                       | 0.920             |
| 30  | 1        | 872010                                       | 3.216             |
| 30  | 2        | 885705                                       | 1.695             |
| 30  | 3        | 892694                                       | 0.920             |
| 20  | 1        | 879655                                       | 0.236             |
| 20  | 2        | 889049                                       | 0.132             |
| 20  | 3        | 894426                                       | 0.072             |

The number of point clouds before denoising is 900991/piece.

For the denoising algorithm in the present study, the confusion matrix method is used to calculate the accuracy rate  $P$  and the recall rate  $R$  of the experimental results to evaluate the effectiveness of the denoising algorithm. The precision rate  $P$  represents the accuracy of the prediction in the result of the positive sample, and the recall rate  $R$  measures the classifier's ability to recognize positive examples. Among them, TP means that the positive class is judged to be a positive class, and the positive class here is a nonnoise point. FP means that the negative class is judged to be a positive class. FN means that the positive class is judged to be a negative class. TN is judged to be a negative class.

$$P = \frac{TP}{TP + FP} \times 100\%, \quad (4)$$

$$R = \frac{TP}{TP + FN} \times 100\%.$$

It can be found that after denoising the fatigue roller contact surface point cloud by using the method in the present study, the isolated points, chamfer edge noise, and

outlier noise in the fatigue roller contact surface point cloud are effectively removed. After comparing the point cloud images of different types of fatigue roller contact surface before and after denoising, it can be found that the point cloud of the fatigue roller contact surface after denoising maintains the basic characteristics of the point cloud model.

In order to compare with traditional denoising algorithms, this paper uses conditional denoising and statistical denoising methods to carry out denoising experiments on the contact surface of the fatigue roller. Table 2 shows the accuracy rate  $P$  and the recall rate  $R$  calculated by using the conditional denoising and statistical denoising algorithms, respectively. Figure 9 is the comparative effect diagram of a fatigue roller with a contact surface width of 4 mm after using conditional denoising and statistical denoising.

Upon comparison of Tables 2 and 3, the precision rate  $P$  and the recall rate  $R$  in the conditional denoising or statistical denoising algorithm are lower than those of the fatigue roller surface point cloud denoising algorithm based on conditions and statistics. In addition, according to Figure 9, the solitary point and chamfer edge noise can basically be removed after the conditional denoising of the fatigue roller contact surface. Nonetheless, the noise near the fatigue defect has not been effectively removed, especially the internal separation of the fatigue defect. Group noise still exists. Besides, the outlier noise inside the fatigue defect is effectively removed after using statistical denoising to denoise the point cloud of the fatigue roller contact surface. Notwithstanding, the isolated point and chamfer edge noise have not been removed. In this regard, it has been inferred that the cloud denoising algorithm has a more obvious denoising effect on the point cloud of the fatigue roller contact surface, enhancing the denoising efficiency and laying the foundation for the subsequent 3D topography reconstruction.

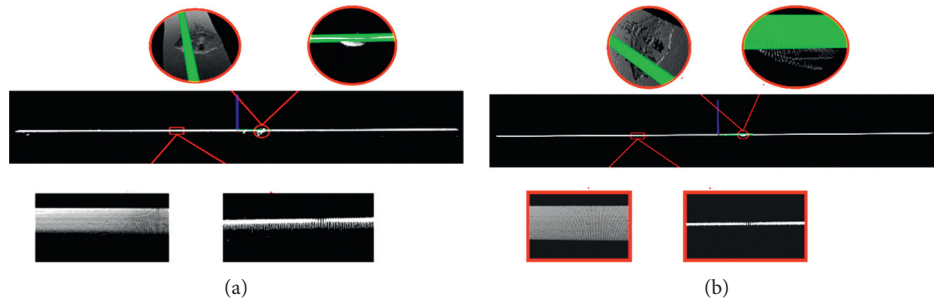


FIGURE 5: The results of point cloud denoising for the roller with a contact surface width of 4 mm. (a) Point cloud before the denoising roller and (b) point cloud after the denoising roller.

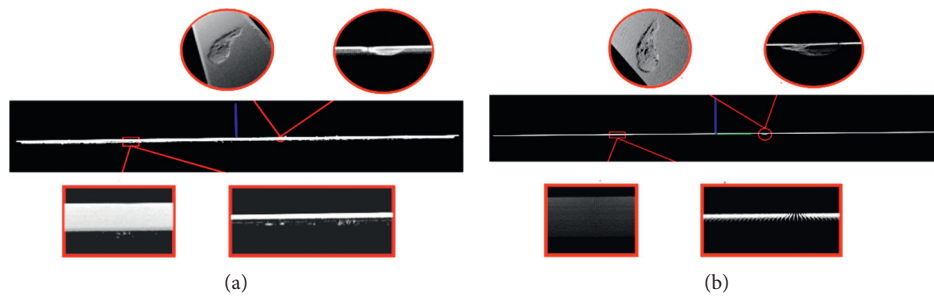


FIGURE 6: The results of point cloud denoising for the roller with a contact surface width of 5 mm. (a) Point cloud before the denoising roller and (b) point cloud after the denoising roller.

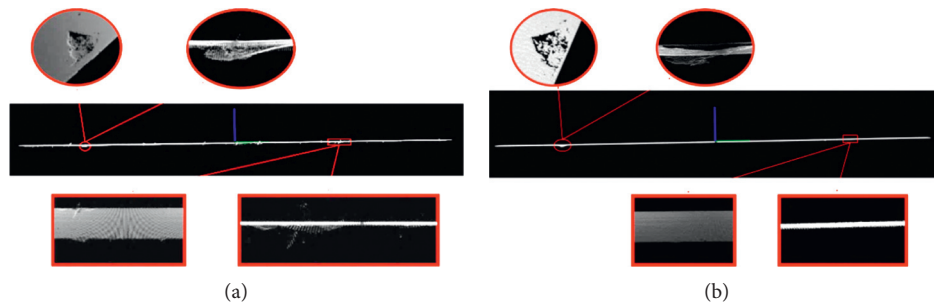


FIGURE 7: The results of point cloud denoising for the roller with a contact surface width of 6 mm. (a) Point cloud before the denoising roller and (b) point cloud after the denoising roller.

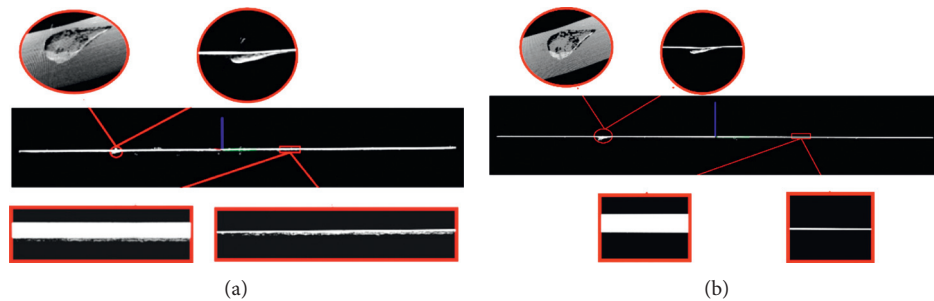


FIGURE 8: The results of point cloud denoising for the roller with a contact surface width of 10 mm. (a) Point cloud before the denoising roller and (b) point cloud after the denoising roller.

4.3. *Reconstruction Verification of the 3D Topography of the Fatigue Roller Surface.* The method in the present study was used to test the selected four different rolling contact fatigue

rollers. The point cloud models are shown in Figure 10(a), and reconstruction results are shown in Figure 10(b), the deviation analysis of the results of the contact surface

TABLE 2: Calculation of precision rate  $P$  and recall rate  $R$  by using conditional denoising or statistical denoising.

| Data group | Type        | TP      | FP   | FN    | TN   | $P$    | $R$ (%) |
|------------|-------------|---------|------|-------|------|--------|---------|
| ①          | Conditional | 810573  | 1054 | 10179 | 280  | 99.87% | 98.76   |
|            | Statistical | 809714  | 1185 | 11038 | 189  | 99.85% | 98.66   |
| ②          | Conditional | 881565  | 1528 | 9853  | 5891 | 99.83% | 98.89   |
|            | Statistical | 880870  | 1835 | 10548 | 5584 | 99.79% | 98.82   |
| ③          | Conditional | 1181535 | 3254 | 8876  | 1196 | 99.73% | 99.25   |
|            | Statistical | 1179126 | 4025 | 11285 | 425  | 99.66% | 99.05   |
| ④          | Conditional | 2014943 | 2217 | 14526 | 7101 | 99.89% | 99.28   |
|            | Statistical | 2014027 | 3856 | 15442 | 5462 | 99.81% | 99.24   |
| ⑤          | Conditional | 881393  | 4421 | 17254 | 293  | 99.5%  | 98.08   |
|            | Statistical | 878101  | 4620 | 20546 | 94   | 99.48% | 97.71   |
| ⑥          | Conditional | 833937  | 1115 | 8896  | 481  | 99.87% | 98.94   |
|            | Statistical | 831380  | 1420 | 11453 | 176  | 99.83% | 98.64   |
| ⑦          | Conditional | 908116  | 3051 | 12549 | 2002 | 99.67% | 98.64   |
|            | Statistical | 907141  | 1853 | 13524 | 3200 | 99.79% | 98.53   |
| ⑧          | Conditional | 791856  | 2569 | 11548 | 1767 | 99.68% | 98.56   |
|            | Statistical | 788164  | 2485 | 15240 | 1851 | 99.69% | 98.1    |

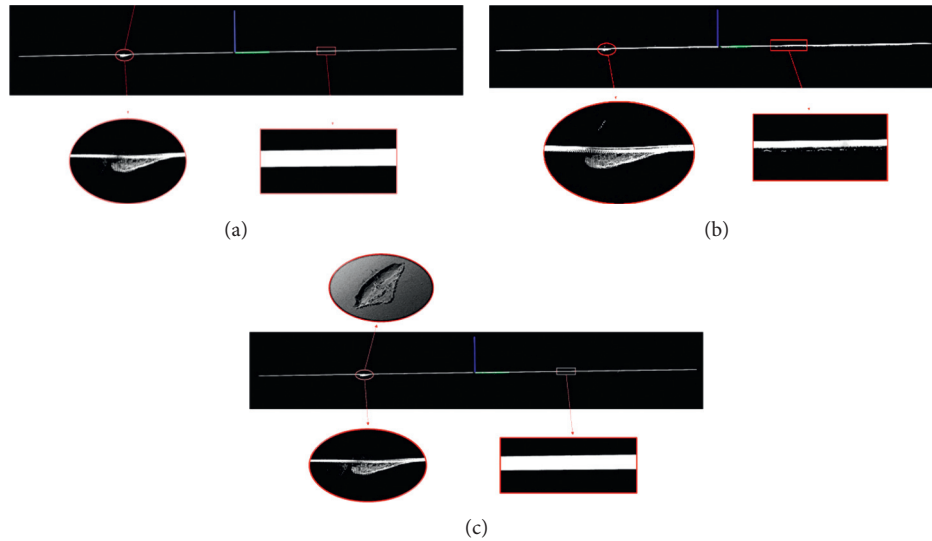


FIGURE 9: The results of point cloud denoising for roller with the contact surface width of 4 mm. (a) The result by using conditional denoising. (b) The result by using statistical denoising. (c) The result by using the conditional and statistical method.

TABLE 3: Calculation of precision rate  $P$  and recall rate  $R$  of the denoising algorithm in the present study.

| Data group | TP      | FP   | FN  | TN   | $P$    | $R$ (%) |
|------------|---------|------|-----|------|--------|---------|
| ①          | 820700  | 72   | 52  | 1302 | 99.99% | 99.99   |
| ②          | 891302  | 50   | 116 | 7369 | 99.99% | 99.98   |
| ③          | 1190301 | 1095 | 110 | 3355 | 99.91% | 99.99   |
| ④          | 2029413 | 72   | 56  | 9246 | 99.99% | 99.99   |
| ⑤          | 898578  | 2656 | 69  | 2058 | 99.71% | 99.99   |
| ⑥          | 842751  | 88   | 82  | 1508 | 99.98% | 99.99   |
| ⑦          | 920546  | 802  | 119 | 4251 | 99.91% | 99.98   |
| ⑧          | 803362  | 510  | 42  | 3826 | 99.94% | 99.99   |

reconstruction of these four types of fatigue rollers were performed, and the results are shown in Figure 10(c). By comparing the model renderings of each roller, the method

in the present study can use the three-dimensional point cloud data obtained by scanning to effectively segment the fatigue rollers with different widths and different fatigue effects. In this way, the outlier noise can be removed in a better way. In addition, the curling of the point cloud image was realized, and a high-quality three-dimensional model of the contact surface of the fatigue roller was finally reconstructed.

The result of the comparison of the measured value of the standard fatigue contact surface width with the segmented fatigue contact surface width model value is shown in Figure 11. The root mean square error between the two is 0.0497 mm. According to statistics, the error range of the fatigue contact surface width after segmentation is 0%–2.3%, most of which are between 0 and 1%. The accuracy of the contact surface segmentation model is relatively high, thus

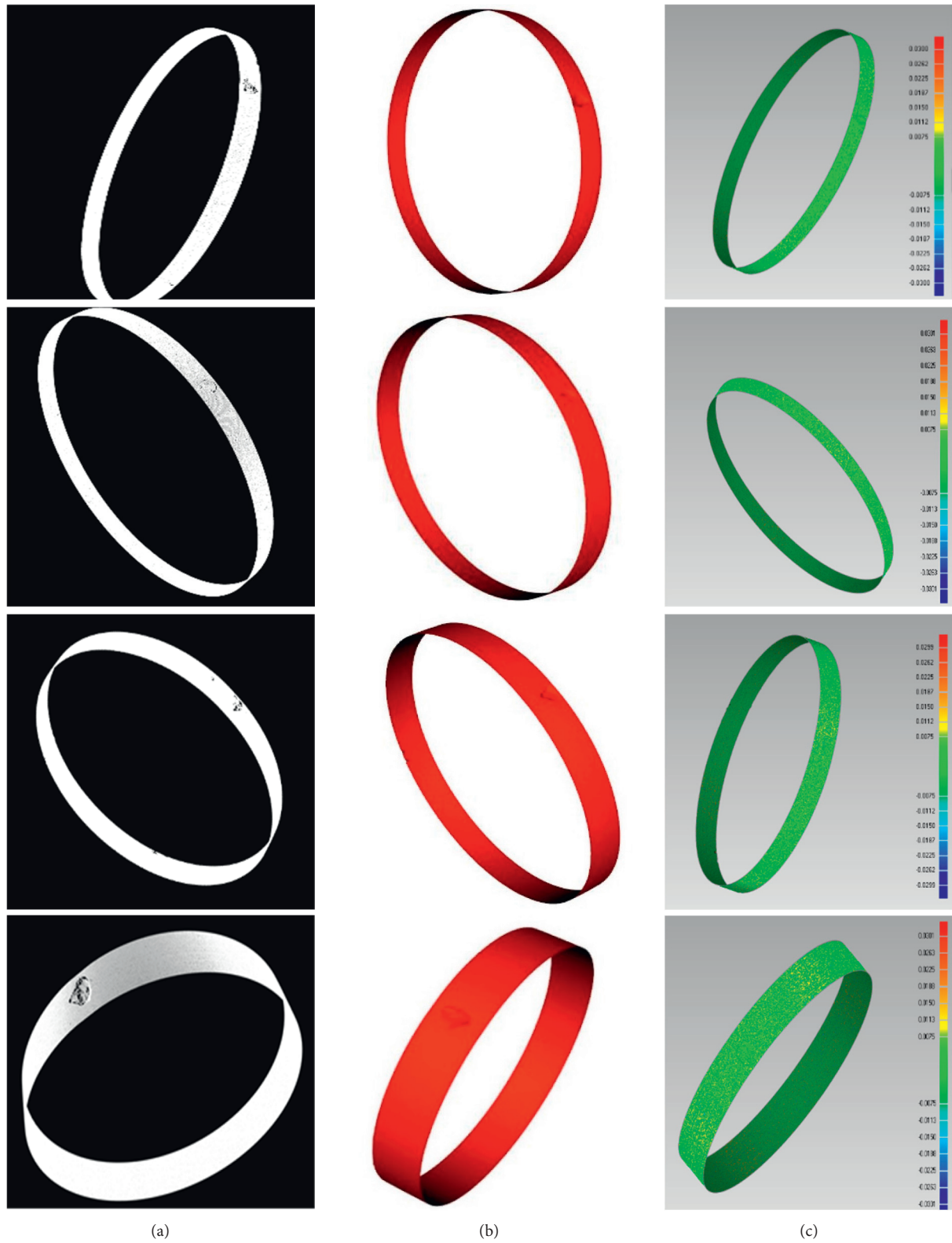


FIGURE 10: Point cloud reconstruction and deviation diagram of different fatigue roller contact surfaces. (a) Point cloud before reconstruction of different roller contact surfaces, (b) reconstruction results of different roller contact surfaces, and (c) reconstruction deviation diagram of different roller contact surface.

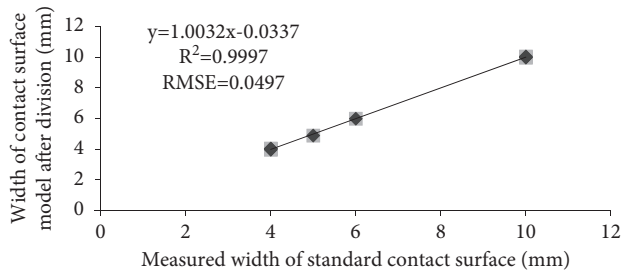


FIGURE 11: Accuracy analysis of the segmentation model of the fatigue roller contact surface.

directly reflecting the segmentation accuracy of the fatigue roller contact surface. According to the point cloud denoising method and the denoising model, as  $K = 30$ ,  $\alpha = 2$ , the outlier noise removal effect tends to be the best. It can effectively remove the outlier noise for different fatigue rollers. Statistics of the number of point clouds before and after curling found that the number of point clouds after curling is exactly the same as the number of point clouds after denoising. It has proven that all points are curled, the radius of the point cloud after curling is 29.97 mm, the curling error rate is 0.09%, and the crimping accuracy is higher. In addition, the analysis results of the deviations of these types of fatigue rollers after reconstruction showed that the maximum deviation is 0.0199 mm. The method in the present study can reconstruct the morphological characteristics of the fatigue rollers well.

## 5. Conclusions

A 3D reconstruction method for fatigue roller specimens based on point cloud data was proposed in this present study. In this 3D reconstruction method, the point cloud data of the roller specimen was collected after fatigue failure through a three-dimensional laser scanner, and then the average  $X$  coordinate of the point where the  $Z$ -axis coordinate changes on the original point cloud image were counted as the point cloud segmentation threshold. Then, the fatigue contact of the roller surface point cloud was segmented, and filtering and denoising preprocessing was conducted on the segmented point cloud. In addition, the point cloud was crimped for the sake of driving the reconstructed 3D model consistent with the actual roller specimen. In the end, the crimped point cloud was greedily triangulated and hole repaired and reconstructed, thereby obtaining high-quality fatigue. Besides, 3D mesh model of the roller surface was used. This method has the following advantages:

- (1) The method proposed in the present study is based on real 3D point cloud data. Hence, the reconstructed 3D model can truly reflect the 3D topography of the roller after fatigue failure.
- (2) The point cloud curling method proposed in the study is also capable of effectively transforming the flat point cloud image into the point cloud image of the revolving body. In this way, the reconstructed 3D model is consistent with the actual roller shape.

- (3) The point cloud data was processed by gridding, and the gridded 3D model was optimized for hole repair to realize the 3D reconstruction of the surface of the roller specimen after failure and effectively retain the shape of the failure surface. These characteristics provide a reliable basis for the later analysis of contact fatigue performance of the roller specimen under the simulated working conditions.

## Data Availability

No data were used to support this study.

## Conflicts of Interest

The authors declare that they have no conflicts of interest.

## Authors' Contributions

Conceptualization was done by Chengkai Zeng; data curation was carried out by Chengkai Zeng and Gaopeng Xu; formal analysis was performed by Chengkai Zeng; funding acquisition was done by Yan Yang; methodology was prepared by Chengkai Zeng; supervision was done by Yan Yang; validation was carried out by Gaopeng Xu and Gang Zhu; visualization was done by Hai Li; writing of the original draft was carried out by Chengkai Zeng; review and editing were conducted by Yan Yang.

## Acknowledgments

This research was funded by the National Natural Science Foundation of China (52075062 and 51875068) and by the National Key Research and Development Program of China (2020YFB2010103).

## References

- [1] M. Kalin and J. Viřintin, "A rolling-contact device that uses the ball-on-flat testing principle," *Wear*, vol. 256, no. 3-4, pp. 335-341, 2004.
- [2] S. W. A. Dekker, "Robert long, jean-luc wybo zero vision and a western salvation narrative," *Safety Science*, vol. 88, 2016.
- [3] V. Manoj, K. Manohar Shenoy, and K. Gopinath, "Developmental studies on rolling contact fatigue test rig," *Wear*, vol. 264, pp. 708-718, 2008.
- [4] M. Endo, S. Okazaki, H. Matsunaga et al., "A new fatigue testing machine for investigating the behavior of small shear-mode fatigue cracks," *Experimental Techniques*, vol. 40, no. 3, pp. 1065-1073, 2015.
- [5] M. Fujii, A. Yoshida, and J. B. Ma, "Rolling contact fatigue of alumina ceramics sprayed on steel roller under pure rolling contact condition," *Tribology International*, vol. 39, pp. 856-862, 2006.
- [6] W. McIlhagga, "Estimates of edge detection filters in human vision," *Vision Research*, vol. 153, pp. 30-36, 2018.
- [7] O. Celik and F. Chuan-Zhi Dong, "Necati Catbas A computer vision approach for the load time history estimation of lively individuals and crowds," *Computers & Structures*, vol. 200, 2018.
- [8] A. Borji, "Negative results in computer vision: a perspective," *Image and Vision Computing*, vol. 69, 2018.

- [9] Q. Shi, L. Chang, C. Wang, H. Luo, Q. Huang, and T. Fukuda, "Design and implementation of an omnidirectional vision system for robot perception," *Mechatronics*, vol. 41, 2017.
- [10] T. L. Schwartz and L. Kelly, "Rebecca Coakley Low vision rehabilitation update: new and innovative 2015," *Journal of AAPOS*, vol. 19, no. 4, 2015.
- [11] J. Radcliffe, J. Cox, and M. Duke, "Bulanon Machine vision for orchard navigation," *Computers in Industry*, vol. 98, 2018.
- [12] S. Shuhan Shen, "Accurate multiple view 3D reconstruction using patch-based stereo for large-scale scenes," *IEEE Transactions on Image Processing*, vol. 22, no. 5, pp. 1901–1914, 2013.
- [13] X. Sun, X. Jiang, Y. Fu, C. Han, and M. Wen, "Camshaft surface defect detection system based on machine vision," *Infrared and Laser Engineering*, vol. 42, no. 06, pp. 1647–1653, 2013, Chinese.
- [14] W. Xie, F. Wang, and D. Yang, "Research on carrot surface defect detection methods based on machine vision," *IFAC-PapersOnLine*, vol. 52, no. 30, pp. 24–29, 2019.
- [15] N. Neogi, D. K. Mohanta, and P. K. Dutta, "Defect detection of steel surfaces with global adaptive percentile thresholding of gradient image," *Journal of The Institution of Engineers (India): Series B*, vol. 98, no. 6, pp. 557–565, 2017.
- [16] H. Xu, F. Keru, L. Huang, L. Xiong, and Z. Yang, "Improved Otsu algorithm for rolling contact fatigue defect detection," *Journal of Computer Aided Design and Graphics*, vol. 31, no. 07, pp. 1130–1138, 2019, Chinese.
- [17] Y. Qu, J. Huang, and X. Zhang, "Rapid 3D reconstruction for image sequence acquired from UAV camera," *Sensors*, vol. 18, no. 1, pp. 225–244, 2018.
- [18] L. G. Roberts, *Machine perception of three dimensional solids*, pp. 71–75, Massachusetts Institute of Technology, Cambridge, MA, USA, 1963, Ph.D thesis.
- [19] N. Snavely, S. M. Seitz, and R. Szeliski, "Photo tourism: exploring photo collections in 3D," *ACM Transactions on Graphics*, vol. 25, no. 3, pp. 835–846, 2006.
- [20] Y. Furukawa and J. Ponce, "Carved visual hulls for image-based modeling," *International Journal of Computer Vision*, vol. 81, no. 1, pp. 53–67, 2009.
- [21] J. Jungong Han, L. Ling Shao, D. Dong Xu, and J. Shotton, "Enhanced computer vision with microsoft kinect sensor: a review," *IEEE Transactions on Cybernetics*, vol. 43, no. 5, pp. 1318–1334, 2013.
- [22] P. Ondr 'uška, P. Kohli, and S. Izadi, "Mobile fusion: real-time volumetric surface reconstruction and dense tracking on mobile phones," *IEEE Transactions on Visualization and Computer Graphics*, vol. 21, no. 11, pp. 1251–1258, 2015.
- [23] M. Pauly, M. Gross, and L. P. Kobbelt, "Efficient simplification of point-sampled surfaces," in *Proceedings of the IEEE Visualization*, pp. 163–170, Boston, MA, USA, October 2002.
- [24] P. Henry, M. Krainin, E. Herbst, X. Ren, and D. Fox, "RGB-D mapping: using Kinect-style depth cameras for dense 3D modeling of indoor environments," *The International Journal of Robotics Research*, vol. 31, no. 5, pp. 647–663, 2012.
- [25] X. I. Wen-Fei, Y. M. Fang, L. Shuai, and L. Jian, "A new research on data compression and simplify technology based on laser scanning point cloud," *Engineering of Surveying & Mapping*, vol. 21, no. 4, pp. 38–40, 2012.
- [26] F. Villa, F. Severini, F. Madonini, and F. Zappa, "SPADs and SiPMs arrays for long-range high-speed light detection and ranging (LiDAR)," *Sensors*, vol. 21, no. 11, p. 3839, 2021.
- [27] S. Nashat, A. Abdullah, and M. Z. Abdullah, "Unimodal thresholding for laplacian-based canny-deriche filter," *Pattern Recognition Letters*, vol. 33, no. 10, pp. 1269–1286, 2012.
- [28] H. Balta, J. Velagic, W. Bosschaerts, G. De Cubber, and B. Siciliano, "Fast statistical outlier removal based method for large 3D point clouds of outdoor environments," *IFAC-PapersOnLine*, vol. 51, no. 22, pp. 348–353, 2018.
- [29] W. Lorensen and H. Cline, "Marching cubes:A high resolution 3D surface construction algorithm," *Computer Graphics*, vol. 21, no. 4, pp. 163–169, 1987.
- [30] F. Wu, J. Li, H. Yang et al., "Research of pavement topography based on NURBS reconstruction for 3D structured light," *Optik*, vol. 194, 2019.
- [31] Y. Quinsat and C. Lartigue, "Filling holes in digitized point cloud using a morphing-based approach to preserve volume characteristics," *International Journal of Advanced Manufacturing Technology*, vol. 81, no. 1-4, pp. 411–421, 2015.
- [32] H. Meng, C. Wang, and Y. Zhang, "A novel hole filling method based on the hybrid PSO-BP algorithm," *International Journal of Computer Applications*, vol. 156, no. 2, pp. 45–50, 2016.
- [33] E. Marchandise, C. Piret, and J.-F. Remacle, "CAD and mesh repair with radial basis functions," *Journal of Computational Physics*, vol. 231, no. 5, pp. 2376–2387, 2012.